Unraveling the electronic properties of graphene with substitutional oxygen

David M.A. Mackenzie[1], Miriam Galbiati[1], Xabier D. de Cerio[2], I. Y. Sahalianov[3], Taras M. Radchenko[4], Jianbo Sun[1], Diego Peña[5], Lene Gammelgaard[1], Bjarke S. Jessen[1], Joachim D. Thomsen[1,6], Peter Bøggild[1], Aran Garcia-Lekue[2,7], Luca Camilli[1,8], José M. Caridad[1,9,*]

[1]Department of Physics and Center for Nanostructured Graphene, Technical University of Denmark, 2800 Kongens Lyngby, Denmark.
[2]Donostia International Physics Center (DIPC), 20018 San Sebastian, Spain.
[3]Laboratory of Organic Electronics, ITN, Linköping University, 60174 Norrköping, Sweden.
[4]Department of Metallic State Theory, G.V. Kurdyumov Institute for Metal Physics of the NAS of Ukraine UA-03142 Kyiv, Ukraine.
[5]Centro Singular de Investigación en Química Biolóxica e Materiais Moleculares (CiQUS), Universidad de Santiago de Compostela, 15705 Santiago de Compostela, Spain.
[6]Department of Materials Science and Engineering, Massachusetts Institute of Technology (MIT), Cambridge, MA, US.
[7]Ikerbasque, Basque Foundation for Science, E-48013 Bilbao, Spain.
[8]Department of Physics, University of Rome "Tor Vergata", 00133, Rome, Italy.
[9]Department of Applied Physics and USAL NanoLab, University of Salamanca, 37008 Salamanca, Spain.

E-mail: `jose.caridad@usal.es`

September 2021

Abstract. We show abrupt changes in the electronic properties of graphene with different types of binding to oxygen. Whereas oxygen bonded to the basal plane in the form of functional groups p-type dopes graphene, we prove that substitutional (i.e. in-plane) oxygen n-type dopes it. Moreover, we determine that impurity scattering potentials introduced by these substitutional atoms are notably larger than those of conventional donors, e.g. nitrogen. Both facts ultimately result in a conduction asymmetry in the system with holes being scattered more strongly than electrons. These findings provide essential insights into the impact of oxygen in carbon nanomaterials such as graphene oxide, oxidized carbon nanotubes or novel two-dimensional π-conjugated organic frameworks, promising compounds for a wide range of applications including flexible electronics, catalysis, energy storage or biomedicine.

1. Introduction

Oxygen-containing carbon nanomaterials such as graphene oxide, GO; oxidized carbon nanotubes or two-dimensional, 2D, organic frameworks, have recently attracted a significant research effort for their potential use in next generation nanoelectronic devices as well as other cutting-edge applications [1-5]. However, both structure and fundamental properties of C and O bonds in all these systems are not yet well known [6,7]. For instance, despite the initial belief of oxygen being exclusively bound to graphene in the form of (out-of-plane) functional groups [1,8], new scanning transmission electron microscopy, STEM, investigations in GO have additionally visualized the presence of different configurations of substitutional oxygen in the hexagonal lattice [9]. The possibility to implant O atoms within an extended sp^2-bonded carbon matrix is further intriguing: some of these heteroatoms (dopants or impurities) consist of triple-coordinated oxygen with three carbon neighbors, bonding configurations which are counterintuitive to the conventional wisdom [9,10].

In the present study, we examine the electronic properties of graphene with substitutional oxygen configurations and reveal substantial differences with respect to the properties of graphene with oxygen-containing functional groups bound to the basal plane. This is done by developing a controlled plasma-based process able to implant oxygen in graphene, in combination with transport, scanning tunneling microscopy, STM, and spectroscopy measurements, and state-of-the-art atomistic calculations.

The manuscript is organized as follows. Section 2 describes the used theoretical and experimental methods, including electronic structure and transport calculations, the implantation of oxygen in graphene via a plasma immersion ion implantation process, device fabrication and electrical and scanning tunneling microscopy measurements. In section 3, we show and discuss our simulation and experimental results. Finally, our conclusions are summarized in section 4.

2. Methods

2.1. Electronic structure calculations

Ab initio calculations were performed using DFT as implemented in the SIESTA code [11], widely used software for the simulation of doped graphene [12]. In order to mimic the experimental conditions, isolated oxygen-based impurities in graphene were simulated using 9×9 graphene supercells containing 162 atoms, i.e. the atomic concentration of dopants is ≈0.5%. Specifically, it is $n_O \times$ 0.5% where n_O is the number of oxygen atoms in the supercells. A vacuum region of 20 Å was included in the direction perpendicular to the graphene layer in order to avoid spurious effects between nonphysical periodic images. Calculations were done using norm-conserving Troullier-Martins pseudopotentials [13] to represent core electrons and a double-ζ polarized (DZP) basis set with 0.01 Ry energy shift to describe valence electrons. Exchange-correlation energies were addressed using the Perdew-Burke-Ernzerhof (PBE) functional [14] within

the generalized gradient approximation (GGA). A 15x15x1 Monkhorst-Pack k-sampling [15] was used to sample the Brillouin zone, and the grid for real space integrations was determined by a 400 Ry cutoff. For all the configurations, both the lattice and the atomic coordinates were fully optimized until the maximal force was below 0.01 eV/ Å and the stress below 0.25 GPa. STM simulations for selected bias intervals, including the resonant states were carried out using the STM utility in SIESTA, which is based on the Tersoff-Hamman approximation [16]. Due to the short-range character of the basis set used by SIESTA, the utility extrapolates the value of the wavefunction out to realistic tip-sample distances. We remark that we use a 9×9 super-cell to avoid the insertion of an artificial gap in the system [17].

2.2. Transport calculations

Numerical calculations of the DC conductivity for different, randomly distributed oxygen configurations and concentrations in graphene lattice are carried out implementing the Kubo-Greenwood formalism. Such formalism is able to capture the qualitative behaviour of all (ballistic, diffusive, and localization) transport regimes and is applicable for systems consisting of millions of atoms [18,19], as it is the case of our experimental devices. Doping and charge carrier scattering introduced by oxygen impurities in graphene are modelled by the following on-site (r_i) potential:

$$V_i = \sum_{j=1}^{N} U_j e^{-|r_i-r_j|^2/(2d^2)}, \tag{1}$$

where N is the number of oxygen dopants occupying j sites with radius-vectors r_j, $d=0.63a$ ($a=0.142$ is the lattice parameter) is an effective potential radius and the potential strenght $U_j=-3\gamma$, with hopping (integral) $\gamma \approx 2.8$ eV. Vacancies are modelled as a site with zero hopping parameters to other sites. We note that the selected d and U_j values produce a good fitting to the DFT calculated results (Figure 1b).

2.3. Implantation of oxygen atoms in graphene

The influence of the kinetic energy on the implantation of oxygen in graphene has been theoretically calculated via molecular dynamics [20]. For a perpendicular angle of incidence, oxygen ions at energies between ∼25-30 eV and ∼100-105 eV have probabilities larger than 10% of being implanted in graphene's basal plane. Moreover, such calculations estimate that the probability to introduce vacancies or in-plane disorder in graphene is low (<1%) with processes undertaken at energies lower than ∼35-40 eV.

In this work, oxygen is implanted in graphene at ∼25 eV by developing a plasma immersion ion implantation, PIII, process. These are versatile and ultra-low energy processes commonly utilized to realize shallow doping in narrow channel devices made from conventional semiconductors [21]. The reactor used for our process has a parallel

plate geometry and a high frequency generator operating at 13.56 MHz is capacitively coupled to the bottom electrode. We use O_2 inlet gas at a constant flow 40 sccm mixed with 5 sccm Ar. We add the 5 sccm Ar to the mixture in order to decrease the breakdown voltage needed to ignite the plasma [21,22] and hereby achieve the desired ultra-low energy irradiation. The pressure in the reactor during the 10 s process is $\sim$30 mTorr, which ensures a low angular dispersion of the ions. In particular, the irradiation is carried out in the collisionless regime (or close to it) since the mean-free path of oxygen ions in plasma is $\sim$1 cm [22] which is similar to the plate separation in our reactor but larger than the sheath thickness for oxygen ions at our working pressure [23,24]. This collisionless regime ensures a narrow energy distribution as well as a small angular dispersion, thus making our process well controlled. Ions in the plasma acquire a kinetic energy ϵ_{kin} given by $\epsilon_{kin} = qV_{DC}$, where q is the ion charge and V_{DC} the DC bias voltage (the latter being the sum of the DC self-bias and the plasma potential). Due to the composition of our plasma (see optical emission spectroscopy measurements, OES, in Supplementary Information), we assume q=1. The required $V_{DC}\sim$25 V is obtained in our PIII process for a platten power P $\sim$ 4.5W. We measure V_{DC} fluctuations $\sim \pm 5$ V during the process.

2.4. Device fabrication

Graphene was mechanically exfoliated onto highly doped silicon wafers with 300 nm of silicon dioxide on top. We use these well-known substrates since they avoid back-sputtering during the oxygen-based plasma treatment [25]. Single layer graphene was identified via optical contrast (Figure 2b) and Raman spectroscopy (Supporting Information).

Stencil devices (so-called device type D1 in our study) are simple two-terminal devices where graphene flakes are directly contacted by using shadow masks. This avoids channel exposure to chemicals or heat treatments from lithographic processes [26]. In our study, flakes are contacted by depositing 50 nm Au on the graphene. The distance between contacts in all these devices is 30 micrometers.

Instead, devices of type D2 are four-terminal devices each with the same dimensions and fabricated on the same graphene flake. Each of these devices has a different area exposed to the oxygen. Metal electrodes in devices D2 were defined by electron beam lithography, EBL, using a double layer PMMA mask and depositing 5 nm/45 nm of Cr/Au in an electron-beam evaporator. Here, the 5 nm thick Cr is an adhesion film which avoids the removal of metal electrodes during lift-off processes. Lift-off of metal from undesired areas was performed in warm acetone, with wafers being rinsed in deionized water, DIW, and isopropyl alcohol, IPA. Nano patterning circular holes arranged in a triangular lattice with a variable spacing s was then also defined by EBL. To do so, a 40 nm thick layer PMMA was used this time. The EBL pattern was developed in IPA:DIW 7:3 at 5° C for 30 seconds, with IPA used as a stopper. Then, sample was processed with the PIII process, as described above. Finally, the PMMA mask was then removed in acetone.

2.5. Electrical measurements

Electrical measurements were undertaken in a Linkam LN600P stage in dry nitrogen. Prior to the measurements, a thermal treatment of 125 °C was performed to remove possible water from the surface. A constant bias DC voltage V_{DS} was applied between the source and drain contacts and the current I passing through the graphene field-effect transistors was measured for different gate voltages V_g or carrier densities $n = C_{ox}V_g/e$. In the former expression C_{ox} is the oxide capacitance per unit area and e is the elementary charge. We also note that, in our devices (300 nm of silicon dioxide as gate dielectric), the doping levels n for a given shift of the charge neutrality point ΔV_{CNP} are approximately equal to $n \sim 0.072 \cdot 10^{12} \cdot \Delta V_{CNP}$ [cm^{-2}]. Moreover, longitudinal voltages V_{xx} were measured with the current traversing the sample in devices of type D2 in order to accurately obtain the conductivity σ and mobility μ of these devices via 4-terminal measurements. Carrier mobility μ in our devices was calculated at carrier concetrations $\pm 5 \times 10^{11}$ cm^2 (or equivalently, voltages $\sim \pm 7$ V) away from the charge neutrality point using:

$$\mu = \frac{d\sigma}{dV_g} \frac{L}{C_{ox} \cdot W} \tag{2}$$

where L and W are the length and width of the measured device area (i.e. region between voltage probes).

2.6. Scanning Tunneling Microscopy measurements

STM measurements were performed with etched-W tips at a base pressure $< 2 \times 10^{-10}$ mbar and a temperature of 9-10 K using an Infinity system (Scienta Omicron). The measurements were taken in constant current mode by applying a bias voltage to the sample. Prior to the STM measurements, the sample was annealed in vacuum at a temperature of 500 °C to remove possible atmospheric adsorbates on the sample.

3. Results and discussion

3.1. Atomistic calculations

Figure 1a shows the relaxed atomic structure of two stable and observed [9] configurations of oxygen implanted in graphene, calculated via Density Functional Theory, DFT. These configurations are: *i*) graphitic substitution (here called configuration C1), where oxygen binds to the three neighbour carbon atoms (i.e. graphitic oxygen); and *ii*) pair of oxygen atoms substituting two nearest neighbour carbon atoms (configuration C2). The top panel of Figure 1a also shows the charge redistribution induced by the O substitution in configuration C1. Briefly, a localized electron depletion is shown at carbon atoms bonded to oxygen (blue color), while an extended (and overall larger) electron accumulation appears at remaining neighbouring
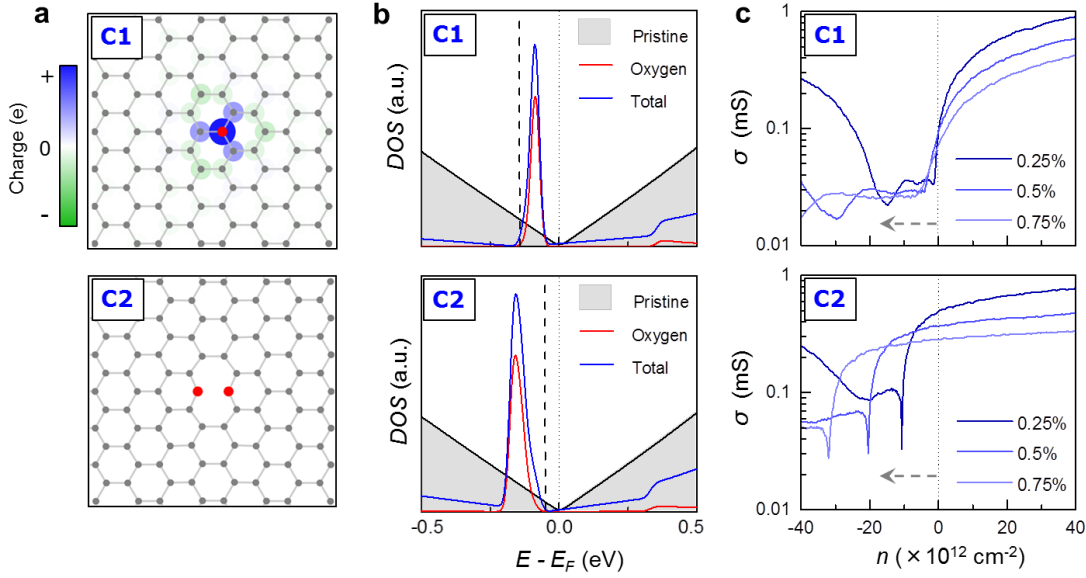
Figure 1: Calculated atomic configurations, electronic and transport properties of graphene with in-plane oxygen dopants. a), Stable and representative [9] atomic configurations of oxygen impurities in graphene, here named C1 (top) and C2 (bottom). Charge balance in configuration C1 is calculated via Hirshfeld atomic populations. b), Density of states (DOS) of pristine graphene (grey) and graphene with in-plane oxygen (blue) for configurations C1 and C2 (red line is DOS projected on oxygen atoms). Vertical dashed and dotted lines correspond to the Dirac point E_D and the Fermi level of graphene with the dopants, respectively. All contributions to the DOS were scaled for visualization purposes. c), Calculated conductivity σ as a function of the carrier density n for different concentrations (shades of blue) of oxygen impurities (configurations C1,C2) in graphene.

carbon atoms (green color). Such behaviour is generic and also occurs in configuration C2 and more complex (and also possible [9]) configurations with vacancies involved (see additional details and Figures S1-S3 in Supporting Information). These evidences indicate that substitutional oxygen is an electron donor, which can be intuitively related to the fact that oxygen has more valence electrons than carbon.

Figure 1b shows the DFT calculated total density of states, DOS, (blue line) and the DOS projected onto oxygen atoms (red line) for the two highlighted configurations C1 and C2, all plotted against the DOS of pristine graphene (grey area). The overall effect of oxygen dopants in graphene is to separate the Dirac point, E_D, (dashed line) away from the Fermi level, E_F, shifting it towards negative values (E_F is set to 0 eV in our calculations). This behaviour is directly related to the fact that in-plane oxygen n-type dopes graphene, evidence that is also clearly observed in the bandstructures of these systems shown in Figure S4, Supporting information. Furthermore, substitutional oxygen introduces sharp resonant states with peaks at energies E_{res} close to E_D (i.e. at low energies), fact that can be ascribed to a strong perturbing potential introduced by substitutional oxygen in graphene [27] (see further details below and in Supporting

Information). In particular, these resonances appear at energies $|E_{res} - E_D| = 0.05$ eV and 0.1 eV for cases C1 and C2, respectively.

Figure 1c contains tight-binding, TB, calculations of the conductivity as a function of carrier density n for graphene devices with configurations C1 and C2 randomly positioned (Figure S6 in Supporting Information) at different concentrations. These simulations allow us to understand the qualitative behaviour of graphene transistors containing these distinct impurities with enough details. Impurity scattering in the TB calculations (obtained as best fit to the DFT calculated local *DOS*, see Figure S5 in Supporting Information) is an attractive, strong and primarily short-range perturbing potential with a depth of 8.4 eV (further details about the impurity potential are described Supporting Information). First, Figure 1c shows a net n-type doping in devices containing both configurations as demonstrated by the left-shift of the conductivity minimum (or charge neutrality point, V_{CNP}) when increasing the concentration of oxygen dopants (grey arrows). Moreover, an overall lower conductivity of both electrons and holes is observed for larger concentration of oxygen impurities, as a result of increased scattering in the device. In more detail, the conductivity suppression is particularly marked at low energies (or carrier densities), which is a direct consequence of the sharp resonant states occurring close to E_D in these systems. In addition, we also observe a higher conductivity of electrons with respect to holes at large energies (carrier densities). Such transport asymmetry is not induced by resonant-scattering but can be ascribed to doping fluctuations occurring in the device due to the randomly distributed n-type (oxygen) dopants in graphene [28,29].

Intriguingly, some of the trends observed for substitutional oxygen are distinctly different from conventional n-type dopants in graphene such as nitrogen. Nitrogen heteroatoms are weaker impurities (potential depth [17] $\sim$3 eV) and therefore introduce broader resonances peaking at energies E_{res} further away from E_D [27] ($|E_{res} - E_D| > 0.2$ eV in most of the configurations containing substitutional nitrogen [17,30]). In turn, electron-hole asymmetry for energies up to 1 eV in graphene with substitutional nitrogen is principally inherited from the resonant-scattering-induced asymmetry in the underlying scattering rate [31]; and therefore a larger hole conductivity/mobility occurs in graphene devices with nitrogen dopants [18,31]. The latter has been already demonstrated in experiments [32]. We further highlight that n-type doping and lower conductivity/mobility of hole carriers are also distinctive characteristics with respect to other cases such as the presence of out-of-plane oxygen-containing functional groups, vacancies or molecular oxygen. Oxygen functional groups bonded to the basal plane are well-known to p-type dope graphene [33,34] due to the larger electronegativity of O atoms (which tend to pull electrons from C atoms and leave holes in the 2D hexagonal lattice [35]). Vacancies or adsorbed molecular oxygen cannot explain these distinct trends either: whereas vacancies do not dope the monolayer and their presence reduces equally the conductivity/mobility of electrons and holes [36,37], adsorbed molecular oxygen reduces electron mobility and p-type dopes the monolayer [38].
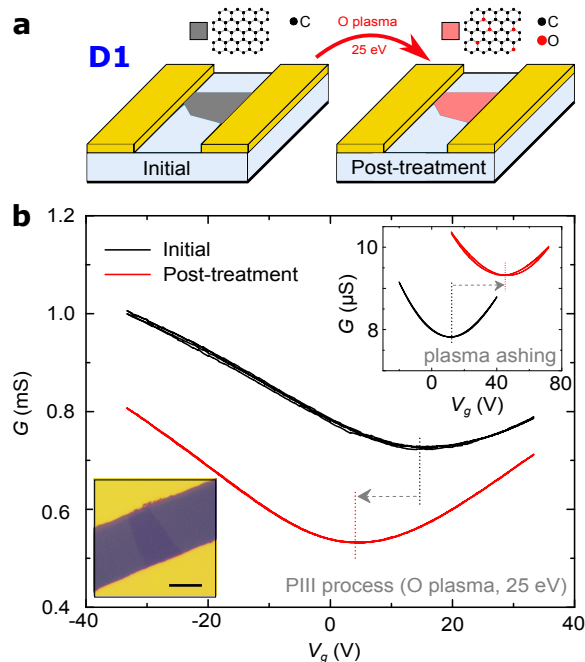
Figure 2: a), Not-to-scale schematic of device type D1. Left panel represents the initial device with as fabricated graphene (grey) and right panel represents the device after graphene was exposed to the here developed ∼25 eV oxygen plasma implantation process (red) b), Conductance measurement of a stencil device subjected to the aforementioned ∼25 eV oxygen plasma implantation process, showing a downshift of V_{CNP} (dashed grey arrow). Upper-right inset: conductance measurement of a stencil device subjected to a downstream oxygen plasma process, showing an upshift of V_{CNP} instead (dashed grey arrow), similar to other reports in literature [33,34]. Lower-left inset: optical image of one of our stencil devices. Scale bar is 20 μm.

3.2. Experimental results and analysis

In the following, we realize and characterize graphene devices with in-plane oxygen dopants, ultimately confirming the aforementioned theoretical predictions. The insertion of oxygen in the graphene lattice is achieved here via irradiation engineering [39], by developing a novel plasma immersion ion implantation [21], PIII, process at a controlled kinetic energy ∼25 eV (Methods). Such ultra-low energy process predominantly introduces in-plane and point-like oxygen impurities in graphene, as confirmed by Raman spectroscopy (Figures S7,S8 in Supporting Information), transport and STM measurements shown below. This is in clear contrast to other oxygen plasma techniques (e.g. plasma ashing at arbitrary energies [33,34]) or common, much less well-controlled wet-chemistry methods used to fabricate GO [1,9], all creating different types of bonding between oxygen and graphene including both, in-plane configurations and out-of-plane functional groups [1,9,33,34]. A more detailed evaluation of our implantation process in terms of density of oxygen and other defects introduced in

the hexagonal lattice, as well as optical emission spectroscopy (OES) data assessing the elemental composition of the plasma, can be found in the Supporting Information.

In order to probe the electronic and transport properties of graphene with in-plane oxygen impurities, we fabricate (details in Methods) two different types of devices (D1 and D2) from exfoliated graphene flakes. All these devices are non-encapsulated [26,40,41], which enable us to measure their electrical properties with and without the oxygen implantation process described above, thus allowing for a direct comparison of results from the same device. D1 (Figure 2a) are simple two-terminal devices where unprocessed graphene flakes are contacted by using shadow masks to avoid channel exposure to chemicals or heat treatments from lithographic processes [26]. These devices are nevertheless sufficient to accurately examine the type and levels of doping in graphene by examining any shift occurring in the charge neutrality point, V_{CNP}, between measurements undertaken before and after any irradiation process [32-34]. In particular, graphene is n-type doped after the controlled $\sim$25 eV oxygen irradiation process, as demonstrated by the significant left-shift (grey dashed arrow) of V_{CNP} (vertical lines) in their conductance, G, vs gate voltage, V_g, graph (Figure 2b). As mentioned above, this trend is a strong evidence pointing towards the implantation of oxygen in the graphene lattice. This behaviour is opposed to the common p-type doping (i.e., right-shift of V_{CNP}) observed for instance when exposing these devices to traditional plasma ashing (see upper-right inset Figure 2b, grey dashed arrow), a process which is known to functionalize graphene with out-of-plane oxygen containing groups [33,34,42]. Moreover, we also highlight that the left-shift of V_{CNP} observed in D1 devices after the $\sim$25 eV oxygen irradiation process is $\Delta V_{CNP} \sim$ 11-14 V. In our devices, these values correspond to variation of doping levels $\sim 10^{12}$ cm^{-2}. Similar doping levels are also estimated from our DFT calculations via $n = \frac{|E_D|^2}{\pi \hbar^2 v_F^2}$, with $|E_D|$ being of the order of $\sim$ 0.1 eV (Figure 1b).

To confirm these observations, we fabricated and measured devices of type D2. These are multiple transistors made from the same graphene flake, where each device has the same dimensions but a different area exposed to the oxygen treatment. The latter is done by using a lithographic nano-patterned mask with a different number of dots (of equal size) in each transistor. Ultimately, all devices have dots arranged in five lines, and the number of dots in each device is controlled by the dot-to-dot distance s (Figure 3a, upper-right inset). Here, we leave one transistor not exposed to oxygen (control device) in order to assess the residual doping of the graphene flake after the lithographic process (Figure 3a, left device). D2 also allows us to accurately estimate the conductivity/mobility values of all channels via 4-terminal electrical measurements. Figure 3b shows the conductivity σ values of the different channel regions vs V_g in devices of type D2 exposed to the $\sim$25 eV oxygen plasma implantation process, confirming the n-type doping already observed in devices D1. In particular, the device not exposed to oxygen irradiation (i.e. control device, black line) shows a residual p-type doping and a larger conductivity/mobility of hole carriers, trends widely attributed to atmospheric contaminants and/or lithography residues [26,33,34]. On the other hand, graphene
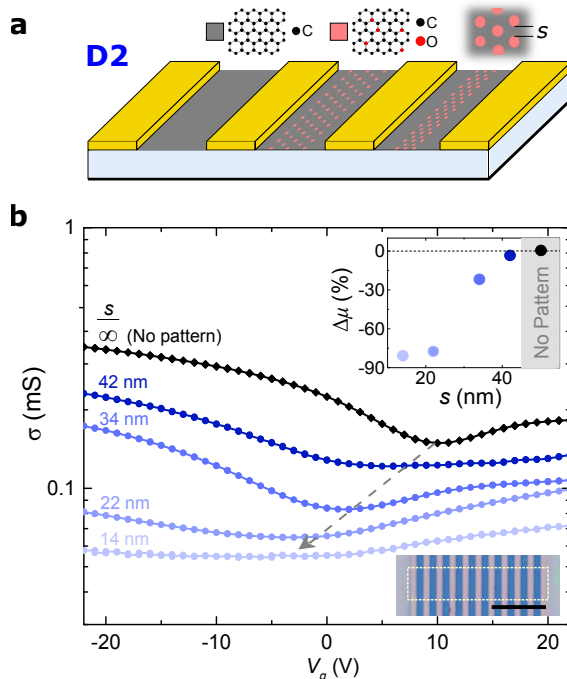
Figure 3: a), Not-to-scale schematic of device type D2. It has non-patterned (top-left) and patterned (top-middle, top-right) devices with different number of nano-dots. b), σ vs V_g for different devices of the study. Regions with a larger area exposed to the $\sim$25 eV oxygen implantation have a higher number of circular dots. To do so, all patterned devices have 5 lines of dots with different separation distances s (legend). Four devices are shown here with separation distances $s = 14$, 22, 34 and 42 nm, corresponding to the different shades of blue dots. Lower inset shows an optical image of the multi-terminal device, with graphene area marked with dashed line (scale bar is 10 μm). Upper inset shows the normalized mobility difference $\Delta\mu$ between holes h and electrons e, $(\mu_h - \mu_e)/(\mu_h + \mu_e)$ with respect to the non-patterned device (in %) in all devices as a function s.

devices exposed to the $\sim$25 eV process exhibit lower conductivities of both electron and holes and a down-shift of V_{CNP} (i.e. n-type doping, see dashed arrow) which correlate to their total area exposed to oxygen (i.e. smaller s). Quantitatively, the observed left-shifts of V_{CNP} (ΔV_{CNP}) are up to $\sim$14 V. This value corresponds to doping levels $\sim 10^{12}$ cm^{-2}, which is consistent to the values observed in devices D1 and those calculated via DFT (Figure 1b). Additionally, we also observe an asymmetric carrier transport with smaller σ and mobility of holes μ_h with respect to electrons μ_e in the devices with smaller s. All these experimental features are in agreement with the inclusion of different configurations of substitutional oxygen in graphene (Figures 1b,c and Figure S1 in Supporting Information). We also emphasize that all these observations are in line with the fact that in-plane oxygen dopants primarily act as neutral [28] rather than charged impurities: unscreened attractive Coulomb impurities would induce the opposite electron-hole asymmetry [43].

Finally, we have used scanning tunnelling microscopy to examine the implanted oxygen
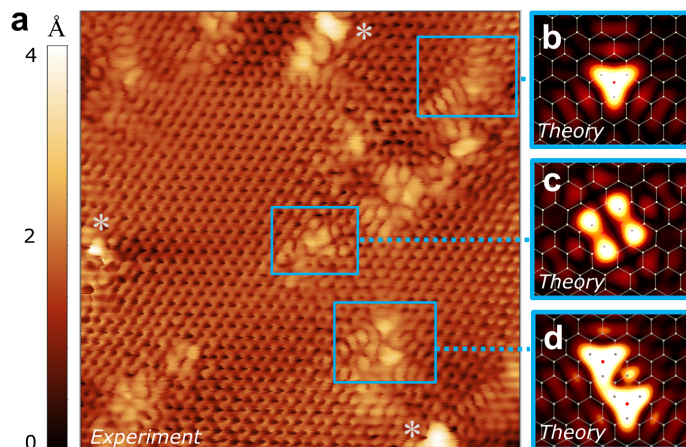
Figure 4: STM image and simulations. a), 8 nm × 8 nm measured STM image (I = 0.5 nA, V = 0.5 V) of highly oriented pyrolytic graphite after the ∼25 eV oxygen irradiation process. Scale-bar indicates the apparent out-of-plane height of the image. From this bar, one can observe that the apparent out-of-plane heights of the identified defects are ∼1 Å. b), DFT-based STM image calculated for single oxygen substitutions, configuration C1 in Figure 1a. c), DFT-based STM image calculated for double pair oxygen substituting two first nearest neighbour carbon atoms, configuration C2 in Figure 1a. d), DFT-based STM image calculated for double pair oxygen substituting two sixth-nearest neighbour carbon atoms. We identify all these defects in the experimental image, panel (a) (see squares). Occasional areas with clustered defects are marked by '*'.

heteroatoms within the hexagonal carbon lattice. For this purpose, we have performed the oxygen irradiation process at ∼25 eV on a ∼1 cm^2 highly oriented pyrolytic graphite (HOPG) sample. Due to the weak interlayer coupling present in graphite, the perturbation induced by point defects in graphene and HOPG systems can be considered equivalent [37]. In fact, graphite is routinely used as model system to reproduce and image the creation of controlled point defects in graphene via STM [44]. Figure 4a reveals areas with pristine honeycomb lattice along with defective regions. Defects have lateral dimensions up to ∼2 nm, compatible with point-like defects and their associated electronic perturbations [37,44,45]. Besides occasional areas with clustered defects (marked by '*'), impurities have apparent out-of-plane heights below 1±0.2 Å, consistent with other previously observed in-plane heteroatoms in the honeycomb lattice [30,46]. The shape of these defects depends on the hexagonal lattice symmetry and the nature of the impurity [30,46,47]. Also, the fact that Figure 4a shows several defects in the hexagonal lattice of HOPG agrees with the large variety of configurations of oxygen in graphene recently visualized in GO via STEM [9] and possible vacancy defects [48] which may occur during our irradiation process. By performing STM-imaging simulations of oxygen atoms in graphene (Figures 4b-d) we are able to identify some of the defects in Figure 4a. For instance, we note the characteristic three- [37,47] and two- [47] fold symmetry features (panels b and c) corresponding to configurations C1 and C2 in Figure 1, respectively. Also, we distinguish a pair of oxygen atoms substituting two

sixth-nearest neighbour carbon atoms (panel d). Moreover, we highlight the importance of configuration C2 to strongly support the effective implantation of oxygen in the lattice by our irradiation process: contrary to the three-fold symmetry of C1, this two-fold symmetry in configuration C2 cannot be created by two neighbour out-of-plane impurities [46], nor by two close vacancies in the hexagonal lattice (Figure S9 in Supporting Information). Moreover, this pattern cannot be created by a chemisorbed epoxy group bonded to two first neighbor carbon atoms in the hexagonal lattice either (configuration which shows a circular pattern [49]). Instead, C2 exhibits a unique pattern resulting only from two first-neighbor heteroatoms implanted in the hexagonal lattice. We note that a comparable pattern is also observed in graphene with two first neighbor substitutional nitrogen atoms [30]. Additional analysis of the STM data shown in Figure 4 can be found in Supporting Information. For completeness, Figure 5a shows scanning tunnelling spectroscopy, STS, measurements of an insolated defect similar to the one shown in Figure 4d. The diferential conductance (dI/dV) data shows resonances at a negative bias. Such resonances are in good agreement with the theoretical DOS calculated in Figure 5b. In particular, by plotting the DOS as a function of the energy (in eV), the peaks of both dI/dV and the DOS appear at the same positions, once more, in clear agreement with the presence of substitutional oxygen in the hexagonal lattice.

4. Conclusions

In conclusion, we have studied the electronic structure and transport properties of substitutional oxygen atoms in graphene by developing a novel and controlled plasma implantation process at ultra-low energy ($\sim$25 eV). Our combined theoretical and experimental study involving complementary techniques such as transport measurements, Raman spectroscopy, STM microscopy and atomistic calculations demonstrates that substitutional oxygen *n*-type dopes graphene and creates an asymmetric conduction in the material with holes being scattered more strongly than electrons. The behaviour of these impurities is thus different to (out-of-plane) oxygen-containing functional groups [33-35] bonded to graphene, which demonstrates how different types of C and O bonds can influence the electronic properties of sp^2 carbon allotropes. From a practical point of view, this understanding is important to assess the impact of oxygen in carbon nanomaterials including graphene oxide and oxidized carbon nanotubes [1,3-5,50], and may be relevant for other related systems such as novel two-dimensional π-conjugated organic frameworks [2]. Moreover, oxygen is ubiquitously present and used to handle and process sp^2 carbon allotropes [1-3,33,34,41,42,51,52]. Therefore, these findings are relevant to move all these nanomaterials from laboratory to industry.
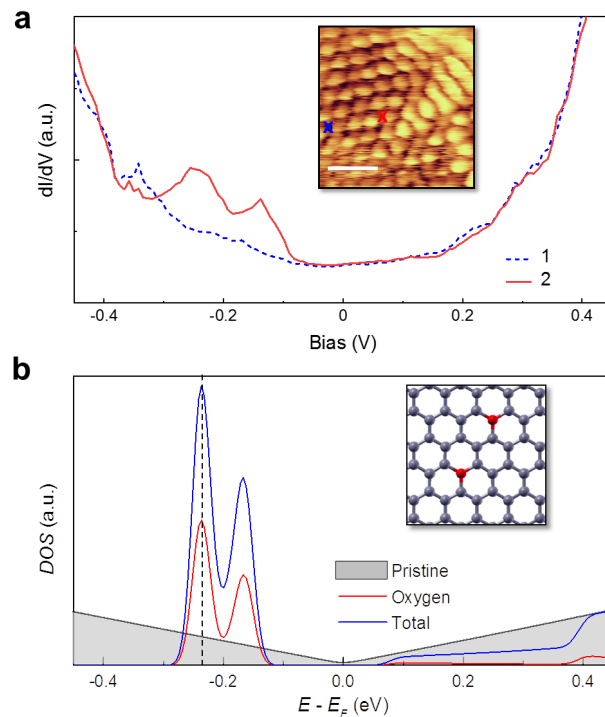
Figure 5: a) STS spectra close to a defect with two oxygen atoms substituting two sixth nearest neighbour carbon atoms, see long range electronic perturbations on the right hand side of the inset. Scale bar in the inset is 0.5 nm. The blue spectrum (dashed line, labeled as "1", positioned at the blue cross in the inset) is taken further away from the defect and has a U shape typical of a pristine graphitic system. Meanwhile, the red spectrum (continuous line, labeled as "2") is taken closer to the defect and shows two main peaks occurring at negative bias ($\sim$ -0.15 and -0.25 V). b) Density of states (DOS) of pristine graphene (grey) and graphene with in-plane oxygen (blue) for a defect consisting of oxygen atoms substituting two sixth-nearest neighbour carbon atoms (see inset). Dashed line indicates the position of the Dirac point. All contributions to the DOS were scaled for visualization purposes.

Acknowledgements

References

[1] Dikin D A, Stankovich S, Zimney E J, Piner R D, Dommett G H B, Evmenenko G, Nguyen S T, Ruoff R S 2007 Preparation and characterization of graphene oxide paper. *Nature*, **448**, 457

[2] Galeotti G, De Marchi F, Hamzehpoor E, MacLean O, Rao M R, Chen Y, Besteiro L V, Dettmann D, Ferrari L, Frezza F, Sheverdyaeva P M, Liu R, Kundu A K, Moras P, Ebrahimi M, Gallagher M C, Rosei F, Perepichka D F, Contini, G 2020 Synthesis of mesoscale ordered two-dimensional π-conjugated polymers with semiconducting properties. *Nat. Mater*, **19**, 874

[3] Ajayan P M, Ebbesen T W, Ichihashi T, Iijima S, Tanigaki K, Hiura H 1993 Opening carbon nanotubes with oxygen and implications for filling. *Nature*, **362**, 522

[4] Jeong H Y, Kim J Y, Kim J W, Hwang J O, Kim J-E, Lee J Y, Yoon T H, Cho B J, Kim S O, Ruoff R S, Choi S-Y 2010 Graphene oxide thin films for flexible nonvolatile memory applications. *NanoLett.*, **10**, 4381

[5] Pei S, Wei Q, Huang K, Cheng H-M, Ren W 2018 Green synthesis of graphene oxide by seconds timescale water electrolytic oxidation. *Nat. Comm.*, **9**, 145

[6] López-Díaz D, López-Holgado M, García-Fierro J L, Velázquez M M 2017 Evolution of the Raman Spectrum with the Chemical Composition of Graphene Oxide. *J.Phys.Chem. C*, **121**, 20489

[7] Skákalová V, Kotrusz P, Jergel M, Susi T, Mittelberger A, Vretenár V, Siffalovic P, Kotakoski J, Meyer J C, Hulman M 2018 Chemical Oxidation of Graphite: Evolution of the Structure and Properties. *J.Phys.Chem. C*, **122**, 929

[8] Wang X, Sun G, Routh P, Kim D-H, Huang W, Chen P 2014 Heteroatom-doped graphene materials: syntheses, properties and applications *Chem. Soc. Rev.*, **43**, 7067

[9] Hofer C, Skákalová W, Görlich T, Tripathi M, Mittelberger A, Mangler C, Monazam M R A, Susi T, Kotakoski J, Meyer J C 2019 Direct imaging of light-element impurities in graphene reveals triple-coordinated oxygen. *Nature Comm.*, **10**, 4570

[10] Vollhardt P, Schore N 2018 Organic chemistry structure and function, Macmillan, New York, USA

[11] Soler J M, Aracho E, Gale J D, García A, Junquera J, Ordejón P, Sánchez-Portal D 2002 The SIESTA method for Ab Initio order-N materials simulation. *J.Phys.: Cond.*

Matter., **14**, 2745

[12] Friedrich N, Prandimarte P, Li J, Saito S, Yamaguchi S, Pozo I, Peña D, Fredereiksen T, Garcia-Lekue A, Sánchez-Portal D, Pascual, J I 2020 Magnetism of topological boundary states induced by boron substitution in graphene nanoribbons. *Phys. Rev. Lett.*, **125**, 146801

[13] Troullier N, Martins J L 1993 Efficient pseudopotentials for plane-wave calculations. *Phys. Rev. B*, **43**, 1993

[14] Perdew J P, Burke K, Ernzerhof M 1996 Generalized gradient approximation made simple. *Phys. Rev. Lett.*, **77**, 3865

[15] Monkhorst J H, Pack J D 1976 Special points for Brillouin-zone integrations. *Phys. Rev. B*, **13**, 5188

[16] Tersoff J, Hamman D R 1983 Theory and application for the scanning tunneling microscope. *Phys. Rev. Lett.*, **50**, 1998

[17] Lambin P, Amara H, Ducastelle F, Henrard L 2012 Long-range interactions between substitutional nitrogen dopants in graphene: electronic properties calculations. *Phys. Rev. B*, **86**, 045448

[18] Radchenko T M, Tatarenko V A, Sagalianov I Y, Prylutskyy Y I 2014 Effects of nitrogen-doping configurations with vacancies on conductivity in graphene. *Phys. Lett. A*, **378**, 2270

[19] Lherbier A, Blase X, Niquet Y M, Triozon F, Roche S 2008 Charge transport in chemically doped 2D graphene. *Phys. Rev. Lett.*, **101**, 036808

[20] Bai Z, Zhang L, Liu L 2015 Bombarding graphene with oxygen ions: combining effects of incident angle and ion energy to control defect generation. *J. Phys. Chem. C*, **119**, 26793

[21] Ziegler J 2012 Ion Implantation Applications, Science and Technology, Academic Press Inc., Elsevier

[22] Chu P K, Qin S, Chan C, Cheung N W, Ko P K 1998 Instrumental and process considerations for the fabrication of silicon-on-insulators (SOI) structures by plasma immersion ion implantation. *IEEE Trans. Plasma Sci.*, **26**, 79

[23] Dittmann K 2009 Thesis, University of Greifswald

[24] Mutsukura N, Kobayasi K, Machi Y 1990 Plasma sheath thickness in radio-frequency discharges. *J. Appl. Phys.*, **68**, 2657

[25] Kolesov E A 2019 Choosing a substrate for the ion irradiation of two-dimensional materials *Beilstein J. Nanotechnol.*, **10**, 531

[26] Gammelgaard L, Caridad J M, Cagliani A, Mackenzie D M A, Petersen D H, Booth T J, Bøggild P 2014 Graphene transport properties upon exposure to PMMA processing and heat treatments. *2D Mater.*, **1**, 035005

[27] Pereira V M, Lopes dos Santos J M B, Castro Neto A H 2008 Modeling disorder in graphene. *Phys. Rev. B*, **77**, 115109

[28] Farmer D B, Golizadeh-Mojarad R, Perebeinos V, Lin Y-M, Tulevski G S, Tsang J C, Avouris P 2009 Chemical doping and electron-hole conduction asymmetry in graphene devices *NanoLett.*, **9**, 388

[29] Caridad J M, Connaughton S, Ott C, Weber H B, Krstić V 2016 An electrical analogy to Mie scattering. *Nat. Commun.*, **7**, 12894

[30] Tison Y, Lagoute J, Repain V, Chacon C, Girard Y, Rousset S, Joucken F, Sharma D, Henrard L, Amara H, Ghedjatti A, Ducastelle F 2015 Electronic interaction between nitrogen atoms in doped graphene. *ACS Nano*, **9**, 670

[31] Kaasbjerg K 2020 Atomistic T-matrix theory of disordered two-dimensional materials: bound states, spectral properties, quasiparticle scattering, and transport. *Phys. Rev. B*, **101**, 045433

[32] Li J, Lin L, Rui D, Li Q, Zhang J, Kan N, Zhang Y, Peng H, Liu Z, Xu H Q 2017 Electron-hole symmetry breaking in charge transport in nitrogen-doped graphene. *ACS Nano*, **11**, 4641

[33] Nourbakhsh A, Cantoro M, Vosch T, Pourtois G, Clemente F, van der Veen M H, Hofkens J, Heyns M M, De Gendt S, Sels B F 2010 Bandgap opening in oxygen plasma-treated graphene. *Nanotechnol.*, **21**, 435203

[34] Childres I, Jauregui L A, Tian J, Chen Y P 2011 Effect of oxygen plasma etching on graphene studied using Raman spectroscopy and electronic transport measurements. *New J. Phys.*, **13**, 025008

[35] Phan, D-T.; Chung, G-S. P-n junction characteristics of graphene oxide and re-

duced graphene oxide on n-type Si(111). *J. Phys. Chem. Solids*, **2013**, 74, 1509

[36] Chen J-H, Cullen W G, Jang C, Fuhrer M S, Williams E D 2009 Defect scattering in graphene. *Phys. Rev. Lett.*, **102**, 236805

[37] Ugeda M M, Brihuega I, Guinea F, Gómez-Rodríguez J M 2010 Missing atom as a source of carbon magnetism. *Phys. Rev. Lett.*, **104**, 096804

[38] Silvestre I, de Morais E A, Melo A O, Campos L C, Goncalves A-M B, Cadore A R, Ferlauto A S, Chacham H, Mazzoni M S C, Lacerda R G 2013 Asymmetric effect of oxygen adsorption on electron and hole mobilities in bilayer graphene: long-and shor-range scattering mechanisms. *ACS Nano*, **8**, 6597

[39] Krasheninnikov A V, Banhart F 2007 Engineering of nanostructured carbon materials with electron or ion beams. *Nat. Mater.*, **6**, 723

[40] Caridad J M, Power S R, Lotz M R, Shylau A A, Thomsen J D, Gammelgaard L, Booth T J, Jauho A-P, Bøggild P 2018 Conductance quantization suppression in the quantum Hall regime. *Nat. Commun.*, **9**, 659

[41] Caridad J M, Power S R, Shylau A A, Gammelgaard L, Jauho A-P, Bøggild P 2019 Gate electrostatics and quantum capacitance in ballistic graphene devices. *Phys. Rev. B*, **99**, 195408

[42] McEvoy N, Nolan H, Kumar N A, Hallam T, Duesberg G S 2013 Functionalization of graphene surfaces with downstream plasma treatments *Carbon*, **54**, 283

[43] Novikov D S 2007 Number of donors and acceptors from transport measurements in graphene. *Appl. Phys. Lett.*, **91**, 102102

[44] López-Polin G, Gómez-Navarro C, Parente V, Guinea F, Katsnelson M I, Pérez-Murano F, Gómez-Herrero J 2015 Increasing the elastic modulus of graphene by controlled defect creation. *Nat. Physics*, **11**, 26

[45] Zhao L, He R, Rim K T, Schiros T, Kim K S, Zhou H, Gutiérrez C, Chockalingam S P, Arguello C J, Pálová L, Nordlund D, Hybertsen M S, Reichman D R, Heinz T F, Kim P, Pinczuk A, Flynn G W, Pasupathy A N 2011 Visualizing individual nitrogen dopants in monolayer graphene. *Science*, **333**, 999

[46] Mizes H A, Foster J S 1989 Long-range electronic perturbations caused by defects using scanning tunneling microscopy. *Science*, **244**, 559

[47] Wehling T O, Balatsky A V, Katsnelson M I, Lichtenstein A I, Scharnberg K, Wiesendanger R 2007 Local electronic signatures of impurity states in graphene. *Phys. Rev. B*, **75**, 125425

[48] Nordlund K, Zinkle S J, Sand, A E, Granberg F, Averback R S, Stoller R E, Suzudo T, Malerba L, Banhart F, Weber W J, Willaime F, Dudarev S L, Simeone D 2018 Primary radiation damage: A review of current understanding and models *J. Nuclear Mat.*, **512**, 450

[49] Hossain M Z, Johns J E, Bevan K H, Karmel H J, Liang Y T, Yoshimoto S, Mukai K, Koitaya T, Yoshinobu J, Kawai M, Lear A M, Kesmodel L L, Tait S L, Hersam M C 2012 Chemically homogeneous and thermally reversible oxidation of epitaxial graphene *Nat. Chem.*, **4**, 305

[50] Zhang G, Duan W, Zhou G, Gu B 2002 The effects of oxygen substitution on the electronic structure of single-walled carbon nanotubes 2002 *Sol. State Comm.*, **122**, 121

[51] Caridad J M, Calogero G, Pedrinazzi P, Santos J E, Impellizzeri A, Gunst T, Booth T J, Sordan R, Bøggild P, Brandbyge M 2018 A graphene-edge ferroelectric molecular switch. *NanoLett.*, **18**, 4675

[52] Rasappa S, Caridad JM, Schulte L, Cagliani A, Borah D, Morris M A, Bøggil P, Ndoni S 2015 High quality sub-10 nm graphene nanoribbons by on-chip PS-b-PDMS block copolymer lithography *RSC Adv.*, **5**, 82, 66711

Unraveling the electronic properties of graphene with substitutional oxygen

Supporting Information

David M.A. Mackenzie[1], Miriam Galbiati[1], Xabier D. de Cerio[2], I. Y. Sahalianov[3], Taras M. Radchenko[4], Jianbo Sun[1], Diego Peña[5], Lene Gammelgaard[1], Bjarke S. Jessen[1], Joachim D. Thomsen[1,6], Peter Bøggild[1], Aran Garcia-Lekue[2,7], Luca Camilli[1,8], José M. Caridad[1,9,*]

[1]Department of Physics and Center for Nanostructured Graphene, Technical University of Denmark, 2800 Kongens Lyngby, Denmark.
[2]Donostia International Physics Center (DIPC), 20018 San Sebastian, Spain.
[3]Laboratory of Organic Electronics, ITN, Linköping University, 60174 Norrköping, Sweden.
[4]Department of Metallic State Theory, G.V. Kurdyumov Institute for Metal Physics of the NAS of Ukraine UA-03142 Kyiv, Ukraine.
[5]Centro Singular de Investigación en Química Biolóxica e Materiais Moleculares (CiQUS), Universidade de Santiago de Compostela, 15705 Santiago de Compostela, Spain.
[6]Department of Materials Science and Engineering, Massachusetts Institute of Technology (MIT), Cambridge, MA, US.
[7]Ikerbasque, Basque Foundation for Science, E-48013 Bilbao, Spain.
[8]Department of Physics, University of Rome "Tor Vergata", 00133, Rome, Italy.
[9]Department of Applied Physics and USAL NanoLab, University of Salamanca, 37008 Salamanca, Spain.

E-mail: `jose.caridad@usal.es`

September 2021

1. Additional DFT calculations

Additional analysis of configurations C1,C2 and other configurations with substitutional oxygen and vacancies

We discuss additional details about the DFT calculated *DOS* of graphene with C1 and C2 configurations, Figure 1b in main text. The position of the resonance E_{res} appears close to but above the Dirac point E_D for configuration C1. This situation resembles the case of a subcritical Coulomb contribution effectively screened within a short distance of the order of the C-C distance a, given the fact that the bound state is occupied (i.e. it lies below E_F). In other words, O dopants in this configuration
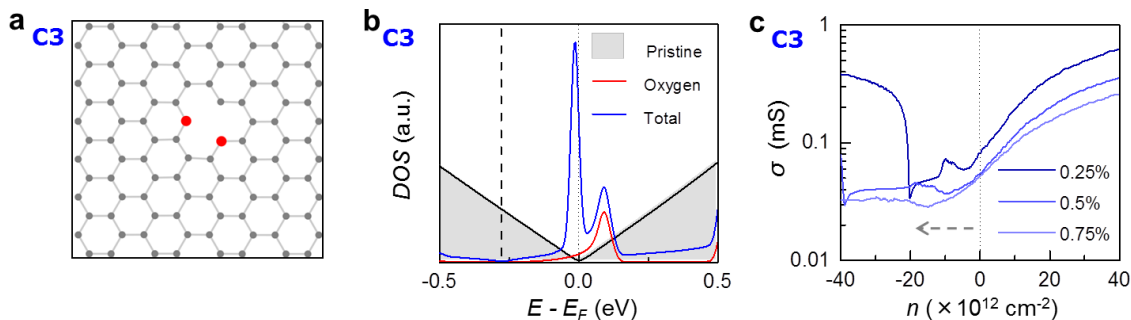
Figure S1: a, Stable and representative [S1] atomic configuration of two substitutional oxygen atoms in graphene close to a vacancy. **b**, Density of states (DOS) of pristine graphene (grey) and graphene with in-plane oxygen (blue) (red line is DOS projected on oxygen atoms).Vertical dashed and dottel lines correspond to the Dirac point E_D and the Fermi level, respectively. All contributions to the DOS were scaled for visualization purposes. **c**, Calculated conductivity σ as a function of the induced carrier density n for different concentrations (shades of blue) of oxygen impurities (configuration C3) in the system.

primarily act as strong, neutral and localized impurities. We remind that, for a single subcritical attractive impurity, $E_{res} > E_D$ and only $E_{res} = E_D$ in the limit of infinite potential strength [S2, S3]. Instead, configuration C2 shows a resonance appearing at a position $E_{res} < E_D$. In principle, this could be due to the fact that the overall charge in configuration C2 is supercritical, situation where itinerant electrons are trapped within a in a sequence of quasi-bound states which resemble an artificial atom [S4, S5]. However, we note that resonances created by a pair of neighboring (short-range) scatterers may appear above or below E_D, depending on the potential strength U [S2]. For attractive perturbing potentials, $E_{res} > E_D$ for small and $E_{res} < E_D$ for large potential strengths, respectively, with the crossing $E_{res} = E_D$ occurring at potentials [S2] $|U| \sim 8\text{eV}$.

Besides configurations C1 and C2 in the main text, substitutional oxygen and vacancies are additional representative configurations [S1]. These type of defects cannot be excluded in our devices: despite our implantation process aims to minimize the insertion of vacancies (see section S5 below), some vacancies could be created during this process. Nevertheless, we show that the main trends reported for the case of configurations C1 and C2 are still valid for configurations containing oxygen and vacancies. Figure S1a shows the DFT calculated relaxed atomic structure of configuration C3, consisting of two oxygen atoms and a vacancy. Figure S1b shows the DOS for this configuration, exhibiting E_D at -0.28 eV and a major peak at an energy -0.025 eV (predominantly due to the vacancy). An additional peak with smaller spectral weight occurs at low positive energies in this case, too. Figure S1c shows the tight-binding calculated conductivity of graphene devices containing this configuration. Similar to cases C1 and C2, configuration C3 also shows a clear *n*-type doping, strong conductance suppression at low energies (carrier densities), and an overall larger conductivity for electrons than holes at large energies (carrier densities).

Charge distributions
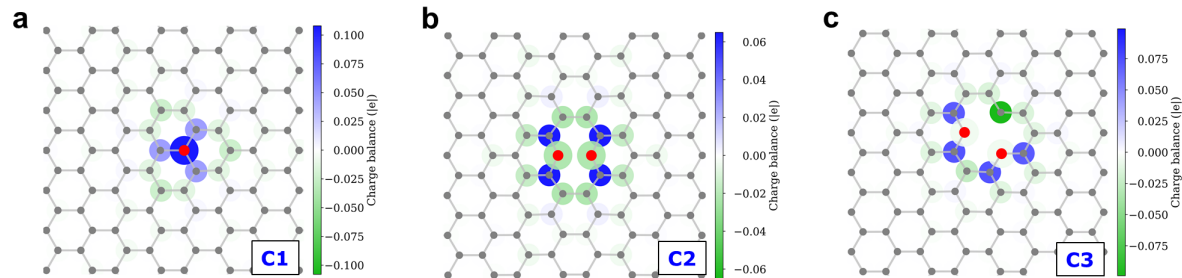
Figure S2: Charge distribution for configurations C1-C3 (see main text and above) calculated with a Hirshfeld population analysis [S6].
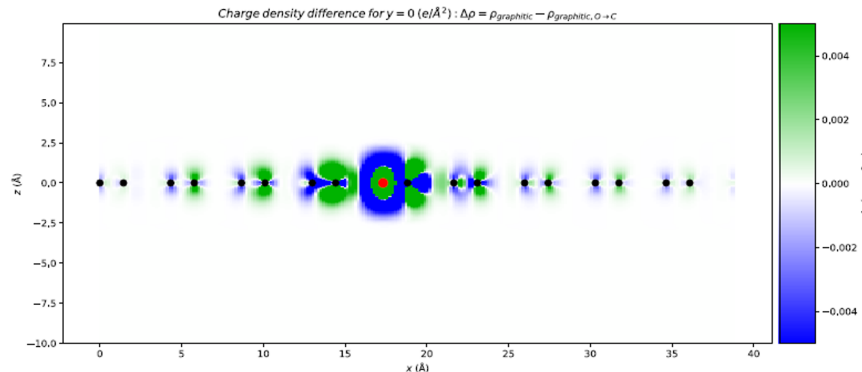

Figure S3: Charge density difference between pristine graphene and graphene with an O dopant ($\rho_{pristine} - \rho_{dopant}$) for configuration C1. Green color indicates here the accumulation of electrons in carbon atoms as a result of the oxygen impurity.

Charge distribution of configurations C1-C3 is performed using the Hirshfeld scheme for partitioning the electron density (Figure S2). By integrating the local charges accumulated over all atoms in the cell of configuration C1 (single oxygen substitution), we obtain 0.107 electrons transferred to the graphene sheet (see a more accurate estimation of net charge transfer in all these configurations in the next subsection). This indicates a small but overall electron accumulation occurring in graphene due to in-plane oxygen. We additionally show the redistribution of charge in the system for configuration C1 (charge density difference between pristine graphene $\rho_{pristine}$ and graphene with the dopant: $\rho_{dopant} = \rho_{pristine} - \rho_{dopant}$). Considering the xz plane (Figure S3), close to the dopant center (x = 22 Å) we observe substantial local changes in the charge, inducing bond polarization effects, similar to the case of substitutional nitrogen [S7] in graphene.

Furthermore, we note that, despite all configurations C1-C3 induce local electron depletion in the C atoms bonded to O, they also exhibit some specific differences which depend on each type of defect. These differences are ascribed to the specific polarization

effects occurring in each configuration. For instance, whereas some of them show a positive charge at the O atom itself (Figure S2a), others show an O with negative charge (Figures S2b,c).

Band structures
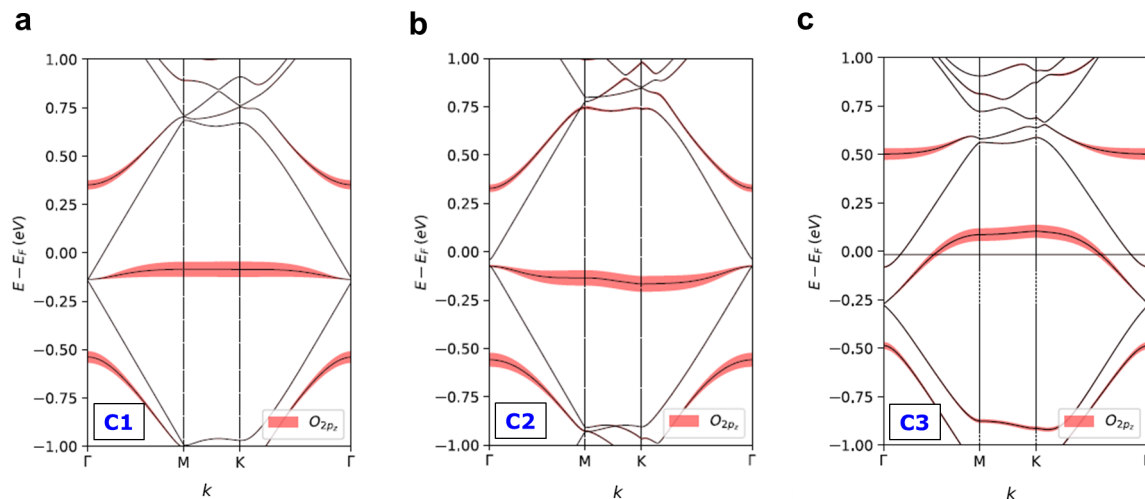
Figure S4: Band structures for configurations C1-C3 (see main text).

Figure S4 shows the calculated band structures for the 3 configurations C1-C3 presented in Figure 1 main text and Figure S1. Overall, in-plane oxygen hybridizes and substantially modifies graphene's bandstructure above and below E_F. We highlight the down-shift of bands (Dirac point, $E_D < 0$ eV) with respect to pristine graphene (case $E_D = E_F = 0$ eV), phenomenon which is once again attributed to electron-doping due to the presence of oxygen in the hexagonal carbon lattice. Doping levels n can be extracted from the position of E_D via $n = \frac{E_D^2}{\pi(\hbar v_F)^2}$, where $v_F \sim 10^6$m/s is the Fermi velocity of charge carriers in graphene. These levels are $\sim 1.46 \times 10^{12}$cm^{-2}, $\sim 2.41 \times 10^{11}$cm^{-2} and $\sim 5.48 \times 10^{12}$cm^{-2} for C1, C2 and C3 configurations, respectively. In terms of net charge transfer, this corresponds to 0.064, 0.011 and 0.24 electrons for C1, C2 and C3, respectively. We observe that configurations C1, C2 show nearly flat electronic bands at negative energies for C1, C2. As shown in the main text, this corresponds to the formation of quasibound states (resonances) at these energies. For completeness, we mention that configuration C3 also exhibits a resonance at low but positive energies $\sim$ +0.15 eV. Such extra peak has a considerably smaller spectral weight than its major peak at -0.025 eV (see DOS calculations in Figure S1b).

2. Simple models of graphene with substitutional oxygen and additional tight-binding calculations

Modelling graphene with substitutional oxygen

In general, heteroatoms in graphene may produce the following interrelated effects [S3, S8]: *i*) dope the monolayer, *ii*) introduce lattice distortions and *iii*) act as scattering centres (including charged-impurity scattering). All these effects can be qualitatively captured within a tight-binding approach by conveniently selecting the hopping amplitude between the dopant and the neighbouring carbon atoms as well as selecting an appropriate impurity potential which may include both short-range and long-range features.[S3, S8, S9] Here, we first focus on the description and justification of a minimal model for a single oxygen substitution in graphene (configuration C1). Then, we use this fundamental building block to understand the effect and model all other impurity configurations (C2,C3) [S10].

In principle, assuming the carbon (C) on-site energy to be the reference state (zero energy), the larger atomic number of oxygen leads to a smaller (and therefore negative) on-site energy U. The presence of such negative on-site energy n-type dopes the monolayer. A local positive charge occurs at the impurity site (see Figure S2a), reason why long-range features may have to be included in the impurity potential. Moreover, O has a smaller atomic radius than C and thus the length of the C-O bond is longer than the one of C-C bonds (according to DFT calculations, the length of a C-O bond is 1.5Å). This fact should be modeled by a hopping integral smaller than the one for C-C bonds $\gamma \approx 2.8$ eV. Nevertheless, the effect of a different hopping integral may be minimal for substitutional impurities consisting of light elements, reason why sometimes this parameter is neglected.[S3, S8]

We also highlight that some of the features exhibited by oxygen impurities (e.g. those concerning the on-site energy, positive local charge and longer C-heteroatom bonds w.r.t. C-C bonds) are qualitatively similar to those of nitrogen dopants [S8, S9, S11]. In particular, both oxygen (Figure 1, main text) and nitrogen [S11, S12] impurities are felt by graphene carriers as attractive perturbing potentials. These potentials always lead to the appearance of resonances above the Dirac point of doped graphene E_D [S3]. However, as highlighted in the main text, resonant states due to oxygen impurities are sharp and appear close to E_D (see Figure 1 main text) due to the strong potential introduced by these heteroatoms in the system. Instead, substitutional nitrogen introduces a weaker impurity potential in graphene resulting in broader resonances occurring further away from E_D [S11, S12]. This fact provokes a qualitatively different carrier scattering behaviour and asymmetries in graphene with both type of impurities for energies up to 1 eV. In order to understand better both similarities and differences between oxygen and nitrogen dopants in graphene, we analyze these two impurities via the simple Lifshitz model.

<u>Lifshitz model</u>. In this framework [S13, S14], substitutional dopants are exclusively

modeled as short-range scatterers by considering the on-site energy shift U at sites occupied by such heteroatoms. The DOS of the system can be calculated as a sum of two parts, host (DOS^h) and impurity (DOS^i) contributions.

Considering an equal sublattice occupancy (i.e. not accounting for a bandgap created in the event of sublattice occupation asymmetry), the contribution of the impurities to the host part DOS^h, [S13] is reduced to a simple shift of the charge neutrality point (Dirac energy level) $E_D = cU$, where c is the impurity concentration. Moreover, the impurity part DOS^i also depends exclusively on U and can be modeled as a resonance positioned at an energy E_{res} (above E_D for $U<0$) defined by the Lifshitz equation [S13, S14]:

$$1 \approx 2\frac{U}{W^2}E_{res}\ln|\frac{E_{res}}{W}| \tag{1}$$

with $W = \gamma\sqrt{\sqrt{3}\pi}$. Despite simple, the Lifshitz model suffices to understand the qualitative behaviour of common impurities in graphene such as nitrogen and boron, which are represented by attractive ($U<0$) or repulsive ($U>0$) potentials and have the resonant position above or below E_D, respectively [S11, S15]. In particular, this model would estimate realistic strengths $|U| < 4\gamma$ in both of these impurities [S16].

In the oxygen case, DFT calculations (Figure 1, where $c \approx 0.5\%$) show the charge neutrality point and the resonance located at a positions $\approx$ -0.14 eV (E_D) and $\approx$ -0.09 eV, respectively (thus $E_{res} - E_D \approx 0.05$ eV). In such situation, the Lifshitz model estimates a $|U|>$ 20-25γ for the impurity band of oxygen to appear at E_{res}. This large value is not unreasonable: a rough atomic-physics estimation would assign U to the difference between the atomic $2p$ levels in O and C, ΔE_{2p}. This difference between the two energy levels would be given by $\Delta E_{2p} \sim -(Z_O^2 - Z_C^2) \times R_h/n^2$, where n=2 and $Z_{O,C}$ are the effective nuclear charges seen by $2p$ electrons in C ($Z_{C:2p}$=3.14) and O ($Z_{O:2p}$=4.45). This leads to $|\Delta E_{2p}| \sim 12\gamma$, magnitude which is not that far from the $|U|$ estimated by the Lifshitz model.

Nevertheless, we note that a tight-binding model using only a single short-range parameter U is not able to precisely reproduce all DFT calculations. This is particularly true for configurations with random distributions of substitutional oxygen of types C2 or C3 (i.e. configurations with two or more close oxygen atoms), pointing towards the need to introduce modifications in the impurity potential [S10, S16].

Short- and long-range interactions. A more refined impurity model including both short-range and long-range interactions can be realized by assuming C on-site energies occupying i sites to vary with the distance to the impurity according to a Gaussian law [S10, S16]. Notably, the long-range term is not a consequence of using an extended perturbation of the on-site energies around the impurity. Instead, it is an interaction term due to the slow decay of the scattering produced by the defect [S16]. Random configurations with two nearby impurities such as C2 can be properly estimated using this model (for the nitrogen case see Refs. [S10, S16]); and this is the main reason why
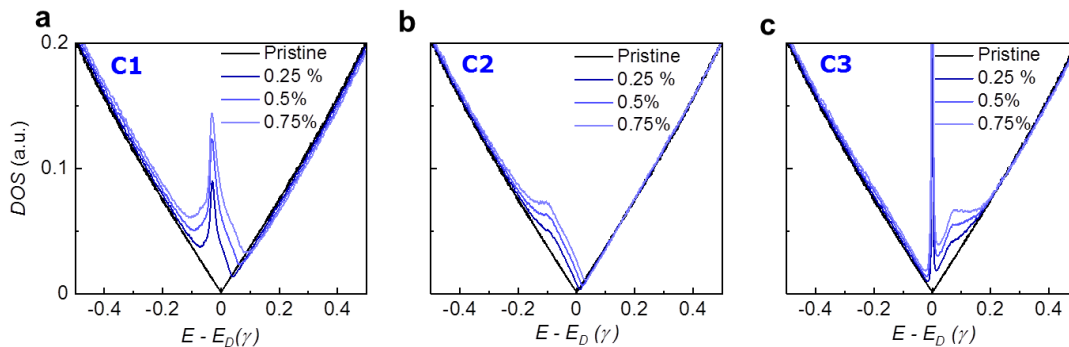
Figure S5: Tight-binding calculated *DOS* for different concentrations of randomly placed configuractions C1 (**a**), C2 (**b**) and C3 (**c**). Parameters to calculate the on-site potential (Eq.2) for all configurations are $|U| = 3\gamma$ eV, $d = 0.63a$. Fermi level in these configuration is at positive energies and can be calculated via $E_F = \hbar v_F \sqrt{\pi n_i c}$, where n_i is the density of impurities in the system and $c \sim 0.1$ is the fraction of charge transferred from these impurities to graphene (calculated in supporting note S1).

we use it in our tight-binding calculations (Figure 1, main text and Figure S1). For attractive impurities, the onsite (r_i) potential is given by:

$$V_i = \sum_{j=1}^{N} -|U|e^{-|r_i-r_j|^2/(2d^2)} \tag{2}$$

where N is the number of oxygen dopants occupying j sites with radius-vectors r_j and d is an effective potential radius which can be interpreted as the screening length. We find relatively good fits to the DFT calculated *DOS* for all configurations C1-C3 for parameters $|U|$ in the range of 3-5γ and d in the range of 0.63-0.47a, with a being the C-C distance (see Figure S5 below). Moreover, as shown in Figure 1c and Figure S1c, the calculation of the conductivity by using this model is able to reproduce our experimental results, too. This good agreement between all DFT and TB simulations and experimental results highlights the fact that *i*) Coulomb centers in graphene with substitutional oxygen are efficiently screened and thus the oxygen potential is primarily short-range ($d < a$). Furthermore, *ii*) substitutional oxygen is reaffirmed to be a notably stronger impurity ($|U| \sim 3\gamma$) than substitutional nitrogen by using this model, too ($|U| \sim \gamma$ for nitrogen using a similar model [S10, S16]).

Scattering potential pattern in graphene lattices with oxygen impurities and calculation of DC conductivity

The main advantage of the Kubo–Greenwood formalism with a tight-binding approximation is the ability to simulate electron transport properties of systems consisting of millions of atoms, and thus model micrometer size devices. In the case of graphene, the implementation of the Kubo–Greenwood method along with the tight-binding approximation allows not only to study systems with extremely low concentrations of defects (0.005%), but also to capture different spatial positions and
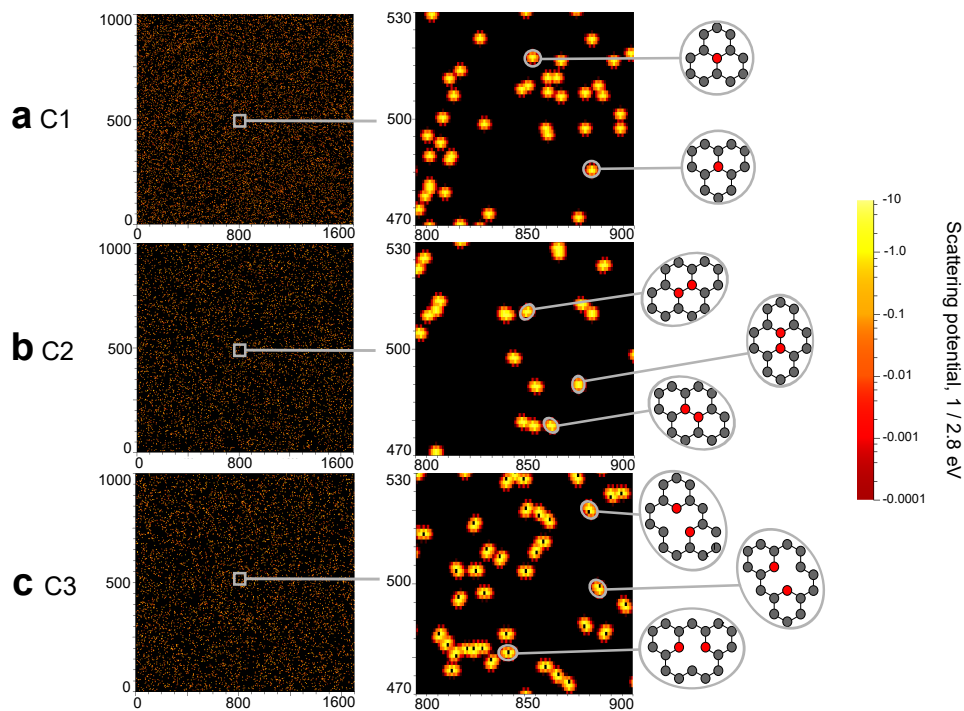
Figure S6: Representative scattering potential distributions in graphene with different configurations of substitutional oxygen-related defects. a) single substitution, C1 (top), b) oxygen pair, C2 (middle), and c) oxygen pair with vacancy, C3 (bottom). Potential is depicted in the hopping integral units (2.8 eV). The first column represents the total graphene lattices used during the simulation (1700×1000 sites). The second column contains zoomed middle regions of the lattices with a size of 100×60 sites, followed by the zoomed pictures of differently oriented oxygen defects. The concentration of oxygen atoms in all plots is 0.5%.

orientation of defects, including the formation of randomly distributed oxygen-rich and defect-free regions, therefore inducing an overall spatially varying potential [S17] as it occurs in our experimental devices. Tight-binding simulations were performed on graphene lattices consisting of 1700×1000 = 1700000 sites.

As aforementioned, a relatively good fit to the DFT calculated DOS is found for parameters $|U| = 3\gamma$ and $d = 0.63a$ (Figure S5). Representative scattering potential distributions calculated for different types of oxygen defects randomly placed in graphene can be found in Figure S6. While the total surface of doped graphene looks similar for all configurations (left column in the Figure S6), the different orientations between defects is apparent in the zoomed regions (middle and right columns). Due to the exponential decay of the potential, the stronger charge carrier scattering occurs on the O sites, and on the the next three nearest-neighboring sites. The scattering potential is negligible for more separates sites.

Finally, the DC conductivity $\sigma(E)$ can be extracted from the DOS and the saturated diffusivity $D_{max}(E)$, when the diffusive transport regime occurs [S10, S15]. The DOS is also used to calculate the electron density $n(E)$ in the system [S10], and thus to obtain $\sigma(n)$ as shown in our calculations.

3. Raman spectroscopy measurements
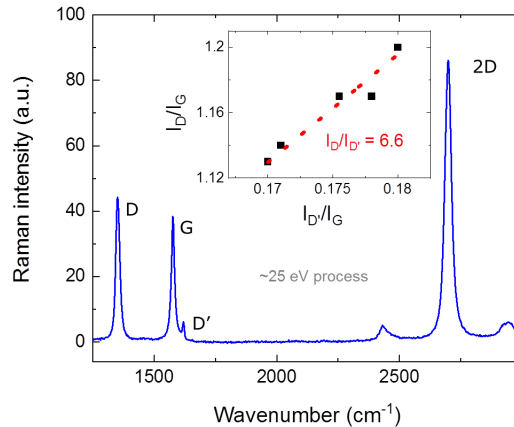
Figure S7: Raman characteristics of graphene devices subjected to our $\sim$25 eV irradiation process. G, 2D, D and D' peaks can be observed. The intensity ratio $I_D/I_{D'} \sim 6.6$ (inset), indicative of sp^2 point defects [S18].

According to Refs.[S18, S19], the nature of defects can be determined via Raman spectroscopy, using the ratio between the intensity of D and D' peaks $I_D/I_{D'}$ occurring in the Raman spectra of defected graphene [S20]. Specifically, one would expect the following ratios:*i*) $I_D/I_{D'} \sim$13 for sp^3 defects such as chemical functionalization; *ii*) $I_D/I_{D'}\sim$7 for sp^2 (i.e. in-plane) point defects such as single-vacancies or in-plane impurities and *iii*) $I_D/I_{D'} \sim$4 for extended (boundary) defects.
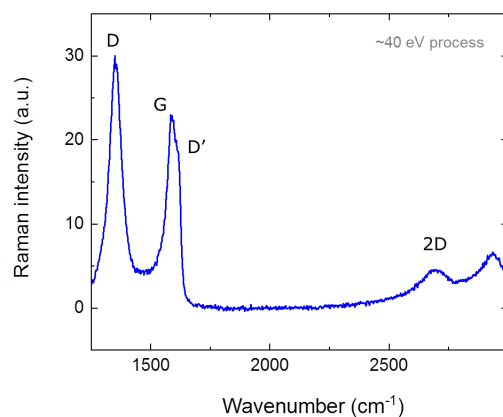
Figure S8: Raman characteristics of graphene devices subjected to a $\sim$40 eV irradiation process. G and D' peaks have roughly the same intensity, indicative of boundary defects [S18].

.

Figure S7 shows Raman spectra from graphene flakes after our $\sim$25 eV oxygen-based plasma process. Here, Raman spectroscopy measurement were performed using a 455 nm excitation and 50x objective. The laser spot size is $\sim$1 μm^2. We notice that,

after the irradiation, the 2D peak [S19] at ~ 2700 cm^{-1} is still noticeable and larger than the G peak at ~ 1585 cm^{-1}. Moreover (Figure S6, inset) the plot of ratios I_D/I_G and I'_D/I_G for different flakes can be fitted to extract a slope (i.e. ratio $I_D/I_{D'}$) ~ 6.6 (close to 7), confirming the predominant presence of sp^2 (in-plane) point defects in our flakes.

Finally, for comparison purposes, Figure S8 shows the Raman spectra of graphene flakes irradiated with our process but an at slightly higher energy (10 secs, ~ 40 eV). These flakes present a residual 2D peak, indicative of considerable amount of defects [S20] in these crystals treated at such higher plasma energies. Furthermore, a much lower ratio $I_D/I_{D'}$ is shown, indicating the presence of boundary defects and large etched regions in the flakes [S18, S19]. This fact emphasizes the importance of the precise bombardment energy ~ 25 eV to implant oxygen in graphene.

4. Additional STM analysis

STM-like image of non-reconstructed di-vacancy defects
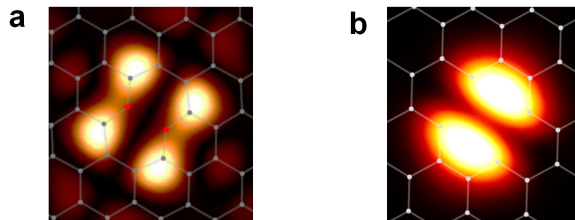
Figure S9: DFT STM-like images of (**a**) two first-neighbour oxygen atoms implanted in the graphene lattice and (**b**) a non-reconstructed double vacancy

We underpin the implantation of in-plane oxygen in graphene by emphasizing that the shape and orientation of some defects shown in Figure 4a, main text, can only be explained byt the presence of in-plane oxygen in our samples. In this sense, we first note that the electronic patterns created by two first neighbor oxygen atoms (configuration C2, see Figure 4c main text, re-plotted in Figure S9a for convenience) are different from the ones created by two out-of-plane impurities [S21] or chemisorbed epoxy group bonded to two first neighbor carbon atoms in the hexagonal lattice either [S22]. Furthermore, we note that the two-fold symmetry pattern shown in Figure S9a cannot be due to the creation of possible (non-reconstructed [S23]) double vacancies during our irradiation process, either. To demonstrate this, Figure S9b shows the calculated STM-like image of a non-reconstructed di-vacancy defect. Although presenting a two-fold symmetry, the orientation of this pattern with respect to the hexagonal lattice does not coincide with the observed experimental feature.
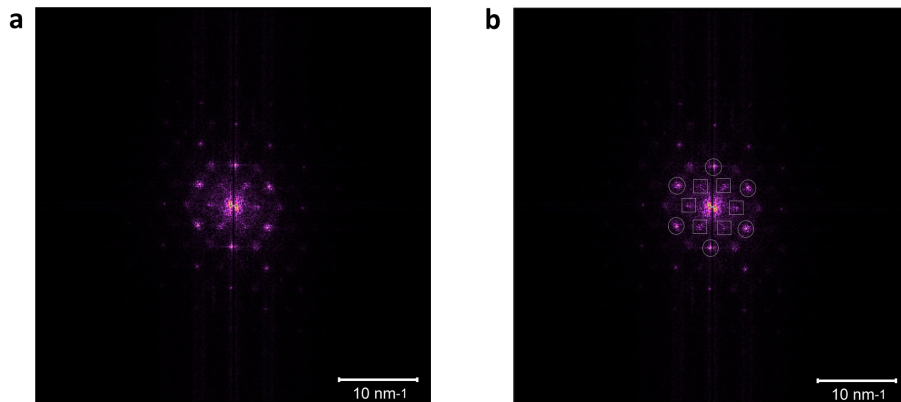
Figure S10: Fourier transform of the image shown in Figure 4a. Panel **b** shows the figure of panel **a**), with two distinct set of spots highlighted by circular and squared shapes (see text).

Fourier transform image and analysis

For completeness, Figure S10 shows the fast Fourier transform (FFT) of the image shown in Figure 4a, main text. This figure contains spots arranged in hexagonal shapes which correspond to relevant the features of the system. Specifically, *i)* the six spots highlighted with circles in panel b) originate from the pristine hexagonal lattice. Meanwhile, *ii)* the six inner spots rotated by 30 degrees w.r.t. the regular hexagonal lattice (squares in panel b)) are due to a $R30°(\sqrt{3} \times \sqrt{3})$ superstructure induced by defects present in the system (such superstructure is visible in Figure 4a in pristine regions of the hexagonal lattice located close to point-defects). Finally, one can also clearly observe additional set of outer spots with the same orientation as those of *ii)* , which are due to the second and third harmonic of the superlattice. All these observations are in agreement with already published works studying point-defects in different graphene-like systems via high-resolution STM images (e.g. [S24,S25]) .

5. Oxygen implantation in graphene via low-energy irradiation. Additional analysis and optical emission spectroscopy (OES) measurements

Additional analysis

As stated in methods, we undertake oxygen implantation in graphene by developing a plasma immersion ion implantation (PIII) process at ultra-low kinetic energy. These are versatile and efficient processes commonly utilized to produce shallow doping in narrow channel devices made from conventional semiconductors [S26], and we use such techniques in the present study to dope graphene with oxygen atoms. In this supplementary section, we include additional details of our process such as estimations of both density of oxygen introduced in the hexagonal lattice and the density of defects.

By taking into account the measured doping levels in our devices $\sim 10^{12}$ cm^{-2} (Figures 2 and 3) and the fact that oxygen in the graphene lattice induces a charge

transfer of $\sim 0.1e$ (see Note 1), we can roughly estimate a density of oxygen introduced in the lattice $\sim 10^{13}$ cm^{-2}. Importantly, this density agrees well with the defect density observed in the STM image, Figure 4a main text (16 point defects in an area of 64 nm^2, density $\sim 2.5 \times 10^{13}$ cm^{-2}).

Regarding in-plane disorder (understood as areas with multiple, clustered defects). From the experimental STM figure placed in the main text (Figure 4a), we can differentiate individual (not clustered) defects with have lateral dimensions up to ~ 2 nm. As aforementioned in the main text, this fact is compatible with point-like defects and their associated electronic perturbations (see Refs. 30,37 and 38 in the main text). We can also distinguish pristine parts of the hexagonal lattice. All these facts indicate that our process is essentially free of multiple (clustered) defects or extended vacancies such as line defects [S27]. This conclusion also agrees with the Raman data shown in Supplementary Section no. 3 (a ratio ID/ID'~ 7 is observed in our flakes after the ~ 25 eV irradiation process, which indicates point-like defects rather than extended defects [S18]).

Finally, regarding the number point-like vacancies introduced in the lattice (e.g. single or double vacancies). We note that the absence of carbon in graphene may lead to multiple reconstructions in the hexagonal [S28]. In Figure 4a (main text), excluding the 3 clustered defects marked with '*', there are 5-6 point defects where the lattice has been reconstructed. This corresponds to a vacancy density of $\sim 9 \times 10^{12}$ cm^{-2}. We note that some of these defects may not contain only vacancies but also oxygen atoms (i.e. these may be configurations with vacancies and oxygen, see an example in Figure S3a).

Optical emission spectroscopy (OES) measurements
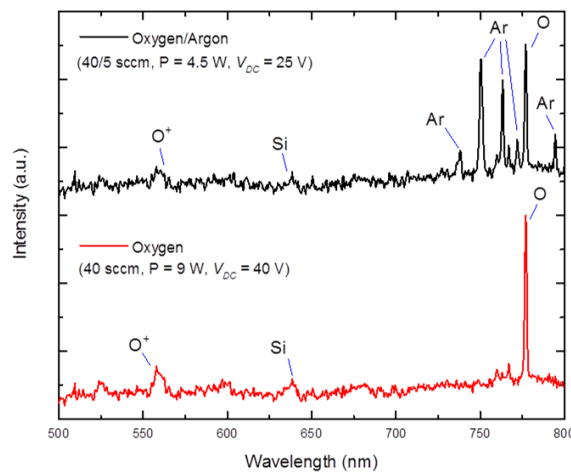
Figure S11: Black line, OES spectra undertaken during the here developed process to implant oxygen in graphene: O/Ar mixture 40/5 sccm at a power P=4.5 W. We additionally show (red line) a similar graph obtained for only a 40 sccm oxygen process at P = 10W for comparison purposes (we remind that the larger power here -10W- is needed to ignite the plasma with only oxygen [S29] in our reactor).

In order to understand better the composition of the plasma, Figure S11 shows optical emission spectroscopy measurements (OES) acquired in our reactor. It clearly shows main peaks at $\sim$777 nm, corresponding to atomic oxygen O, as well as Ar peaks at $\sim$738 nm, $\sim$750 nm, $\sim$763.5 nm, $\sim$772 nm and $\sim$792 nm. [S30] Additional peaks with lower weight are the O^+ peak at $\sim$559 nm [S30, S31] and Si peak at 635 nm [S30] due to the test silicon wafer present in the PIII chamber while measuring OES spectra of our process. We note that the main oxygen peak at $\sim$777 nm is related to excited oxygen atoms O^* decaying with emissions at both $\sim$777 nm and $\sim$845 nm (the latter out of the range of our spectrometer): $O^* \rightarrow O + h\nu$. Such excited states O^* can be explained as a mutual neutralization between positive and negative oxygen ions created in the O_2 based plasma [S32]: $O^+ + O^- \rightarrow O^* + O$.

References

[S1] Hofer C, Skákalová W, Görlich T, Tripathi M, Mittelberger A, Mangler C, Monazam M R A, Susi T, Kotakoski J, Meyer J C 2019 Direct imaging of light-element impurities in graphene reveals triple-coordinated oxygen. *Nature Comm.*, **10**, 4570

[S2] Wehling T O, Balatsky A V, Katsnelson M I, Lichtenstein A I, Scharnberg K, Wiesendanger R 2007 Local electronic signatures of impurity states in graphene. *Phys. Rev. B*, **75**, 125425

[S3] Pereira V M, Lopes dos Santos J M B, Castro Neto A H 2008 Modeling disorder in graphene. *Phys. Rev. B*, **77**, 115109

[S4] Pereira V M, Kotov V N, Castro Neto A H 2008 Supercritical Coulomb impurities in gapped graphene. *Phys. Rev. B*, **78**, 085101

[S5] van Pottelberge R, Moldovan D, Milovanovic S P 2019 Molecular collapse in monolayer graphene. *2D Mater.*, **6**, 045047

[S6] Hirshfeld F 1977 Bonded-atom fragments for describing molecular charge densities. *Theor. Chem. Acta.*, **44**, 129

[S7] Schiros T, Nordlund D, Pálova L, Prezzi D, Zhao L, Kim K S, Wurstbauer U, Gutiérrez C, Delongchamp D, Jaye C, Fishcer D, Ogasawara H, Pettersson L G M, Reichman D R, Kim P, Hybertsen M S, Pasupathy A N 2012 Connecting dopant bond type with electronic structure in n-doped graphene. *NanoLett.*, **12**, 4025

[S8] Peres N M R, Klironomos F D, Tsai S W, Santos J R, Lopes dos Santos J M B, Castro Neto A H 2007 Electron waves in chemically substituted graphene. *Europhys*

Lett., **80**, 67007

[S9] Kaasbjerg K 2020 Atomistic T-matrix theory of disordered two-dimensional materials: bound states, spectral properties, quasiparticle scattering, and transport. *Phys. Rev. B*, **101**, 045433

[S10] Radchenko T M, Tatarenko V A, Sagalianov I Y, Prylutskyy Y I 2014 Effects of nitrogen-doping configurations with vacancies on conductivity in graphene. *Phys. Lett. A*, **378**, 2270

[S11] Joucken F, Tison Y, Le Fèvre P, Tejeda A, Taleb-Ibrahimi A, Conrad E, Repain V, Chacon C, Bellec A, Girard Y, Rousset S, Ghijsen J, Sporken R, Amara H, Ducastelle F, Lagoute J 2015 Charge transfer and electronic doping in nitrogen-doped graphene. *Sci. Rep.*, **5**, 14564

[S12] Wu M, Cao C, Jiang J Z 2010 Light non-metallic atom (B,N,O and F)-doped graphene: a first-principles study. *Nanotechnol.*, **21**, 505202

[S13] Pogorelov Y G, Loktev V M, Kochan D 2020 Impurity resonance effects in graphene vs impurity location, concentration and sublattice occupation. *Phys. Rev. B*, **102**, 155414

[S14] Skrypnyk Y V, Loktev V M 2018 Electronic properties of graphene with point defects. *Low Temp. Phys.*, **44**, 1112

[S15] Lherbier A, Blase X, Niquet Y M, Triozon F, Roche S 2008 Charge transport in chemically doped 2D graphene. *Phys. Rev. Lett.*, **101**, 036808

[S16] Lambin P, Amara H, Ducastelle F, Henrard L 2012 Long-range interactions between substitutional nitrogen dopants in graphene: electronic properties calculations. *Phys. Rev. B*, **86**, 045448

[S17] Farmer D B, Golizadeh-Mojarad R, Perebeinos V, Lin Y-M, Tulevski G S, Tsang J C, Avouris P 2009 Chemical doping and electron-hole conduction asymmetry in graphene devices *NanoLett.*, **9**, 388

[S18] Eckmann A, Felten A, Mishchenko A, Britnell L, Krupke R, Novoselov K S, Casiraghi C 2012 Probing the nature of defects in graphene by Raman spectroscopy *NanoLett.*, **12**, 3925

[S19] López-Polin G, Gómez-Navarro C, Parente V, Guinea F, Katsnelson M I, Pérez-Murano F, Gómez-Herrero J 2015 Increasing the elastic modulus of graphene by con-

trolled defect creation. *Nat. Physics*, **11**, 26

[S20] Ferrari A C 2007 Raman spectroscopy of graphene and graphite: disorder, electron-phonon coupling, doping and non-adiabatic effects. *Solid State Comm.*, **143**, 47

[S21] Mizes H A, Foster J S 1989 Long-range electronic perturbations caused by defects using scanning tunneling microscopy. *Science*, **244**, 559

[S22] Hossain M Z, Johns J E, Bevan K H, Karmel H J, Liang Y T, Yoshimoto S, Mukai K, Koitaya T, Yoshinobu J, Kawai M, Lear A M, Kesmodel L L, Tait S L, Hersam M C 2012 Chemically homogeneous and thermally reversible oxidation of epitaxial graphene *Nat. Chem.*, **4**, 305

[S23] Hashimoto A, Suneaga K, Gloter A, Urita K, Iijima S 2004 Direct evidence for atomic defects in graphene layers. *Science*, **470**, 870

[S24] Ruffieux P, Gröning O, Schwaller P, Schlapbach L, Gröning P 2000 Hydrogen atoms cause long-range electronic effects on graphite *Phys. Rev. Lett.*, **84**, 21, 4910

[S25] Rutter G M, Crain J N, Guisinger N P, Li T, First P N, Stroscio J A 2007 Scattering and interference in epitaxial graphene *Science*, **317**, 219

[S26] Ziegler J 2012 Ion Implantation Applications, Science and Technology, Academic Press Inc., Elsevier

[S27] Lahiri J, Lin Y, Bozkurt P, Oleynik I I, Batzill M 2010 An extended defect in graphene as a metallic wire *Nat. Nanotechnol.*, **5**, 326

[S28] Nordlund K, Zinkle S J, Sand, A E, Granberg F, Averback R S, Stoller R E, Suzudo T, Malerba L, Banhart F, Weber W J, Willaime F, Dudarev S L, Simeone D 2018 Primary radiation damage: A review of current understanding and models *J. Nuclear Mat.*, **512**, 450

[S29] Rhee J K, Moon S Y, Choe W 2007 Change or the argon-based atmospheric pressure large area plasma characteristics by the helium and oxygen gas mixing. *Thin Solid Films*, **515**, 4909

[S30] Herman I P 1996 Optical diagnostics for thin film processing, Academic Press Inc.

[S31] Rezaei F, Abbasi-Firouzjah M, Shokri B 2014 Investigation of antibacterial and wettability behaviours of plasma-modified PMMA films for application in ophthalmology. *J. Phys. D: Appl. Phys.*, 085401

[S32] Ishikawa T, Hayashi D, Sasaki K, Kadota K 1998 Determination of negative ion density with optical emission spectroscopy in oxygen afterglow plasmas. *Appl. Phys. Lett.*, **72**, 2391